nature chemistry

ARTICLES

PUBLISHED ONLINE: 3 MARCH 2013 | DOI: 10.1038/NCHEM.1578

Redox-inactive metals modulate the reduction potential in heterometallic manganese–oxido clusters

Emily Y. Tsui[1], Rosalie Tran[2], Junko Yano[2] and Theodor Agapie[1]*

Redox-inactive metals are found in biological and heterogeneous water oxidation catalysts, but, at present, their roles in catalysis are not well understood. Here, we report a series of high-oxidation-state tetranuclear-dioxido clusters comprising three manganese centres and a redox-inactive metal (M). Crystallographic studies show an unprecedented $Mn_3M(\mu_4\text{-}O)(\mu_2\text{-}O)$ core that remains intact on changing M or the manganese oxidation state. Electrochemical studies reveal that the reduction potentials span a window of 700 mV and are dependent on the Lewis acidity of the second metal. With the pK_a of the redox-inactive metal–aqua complex as a measure of Lewis acidity, these compounds demonstrate a linear dependence between reduction potential and acidity with a slope of ~100 mV per pK_a unit. The Sr^{2+} and Ca^{2+} compounds show similar potentials, an observation that correlates with the behaviour of the oxygen-evolving complex of photosystem II, which is active only if one of these two metals is present.

Redox-inactive metal ions are critical components in many biological electron transfer reactions[1,2]. For example, Ca^{2+} is essential for activity in the oxygen-evolving complex (OEC) of photosystem II (PSII), although its exact role in catalysis remains unclear[3–5]. There have been numerous studies of electron transfer to synthetic organic substrates[1,6], but fewer studies of the electron transfer to metal–oxo complexes relevant to the active sites of a number of metalloenzymes, possibly due to the challenge of isolating complexes with bound metal ions. Recently, a non-haem $Fe^{IV}O$ complex with a bound Sc^{3+} ion was characterized crystallographically, and it was found that the presence of Sc^{3+} or Ca^{2+} in solution allowed the two-electron reduction of the complex using ferrocene[7]. The addition of other Lewis-acidic metal ions to a different $Fe^{IV}O$ compound greatly enhanced electron transfer rates, although the adducts were not structurally characterized[8]. With a monomeric Mn^{II} complex, faster rates of oxygen reduction were observed in the presence of Ca^{2+}, and a $Mn^{III}-(\mu\text{-}OH)-Ca^{II}$ complex was isolated as the product[9]. Substitution of Sr^{2+} for Ca^{2+} in this complex showed a similar reduction potential, while substitution with Ba^{2+} resulted in a more negative reduction potential[10]. Oxygen atom transfer from some manganese–oxo complexes has also been promoted by the binding of redox-inactive metals such as lithium[11].

Redox-inactive metal ions also play a role in non-biological electron transfer reactions such as water oxidation catalysed by heterogeneous cobalt[12–14] and manganese oxides[15–17] containing alkali or alkali earth metals. In these examples, there has been speculation that the redox-inactive metal is associated with the transition-metal catalyst in cubane-like structures reminiscent of the crystallographically determined structure of the OEC, an oxide-bridged $CaMn_4$ cluster in which the calcium centre is associated with three of the manganese centres in a cubane motif (Fig. 1)[18,19]. A recent study varying the redox-inactive metal (K^+, Ca^{2+}, Sr^{2+}, Mg^{2+}) in layered heterogeneous manganese oxides showed that, as in the OEC, the presence of Ca^{2+} allows for the highest catalytic activity[15]. Additionally, heterogeneous mixed oxides of cobalt show different water oxidation behaviour that is dependent on the nature of the redox-inactive metal present in the mixture[20]. The role of the redox-inactive metal on electron transfer and catalysis within the material remains unclear in these systems.

Our recent report of a structural model of the $CaMn_3$ subsite of the OEC containing a high-oxidation-state heterometallic $Mn^{IV}{}_3CaO_4$ moiety, and comparison to a tetramanganese analogue, suggests a significant influence of the calcium centre on the redox properties of the cluster[21]. To study the scope and chemical basis of this phenomenon in multimetallic oxide clusters such as those found in the OEC and in heterogeneous systems, access to well-defined and structurally related heterometallic oxido clusters of redox-active and inactive metals is desirable. Based on a multinucleating ligand-based synthetic strategy developed by our group[22–24], we targeted heteronuclear clusters supported by the hexapyridyl tris-alkoxido 1,3,5-triarylbenzene ligand (L). In the present work, we describe the synthesis of a series of tetranuclear heterometallic trimanganese dioxo clusters $[Mn_3M(\mu_4\text{-}O)(\mu_2\text{-}O)]$ containing a redox-inactive cation bridging via oxido moieties to manganese centres. Electrochemical characterization reveals that large changes

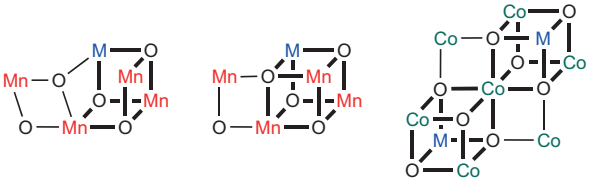

Figure 1 | Proposed structures of water oxidation catalysts containing redox-inactive metals (M) in the OEC (left, middle) and in heterogeneous cobalt oxide water oxidation catalysts (right)[12,43]. The OEC is known to contain a Mn_3M core: one major model is based on extended X-ray absorption fine structure (EXAFS) and electron paramagnetic resonance (EPR) studies (left)[44–46] and one on X-ray crystallography (middle)[18,19]. Bold bonds emphasize the Mn_3M and Co_3M cluster cores.

[1]Division of Chemistry and Chemical Engineering, California Institute of Technology, 1200 East California Boulevard MC 127-72, Pasadena, California 91125, USA, [2]Physical Biosciences Division, Lawrence Berkeley National Laboratory, Berkeley, California 94720, USA. *e-mail: agapie@caltech.edu

in the Lewis acidity of the redox-inactive metal have a systematic effect on the redox properties of the cluster.

Results and discussion

Heterometallic clusters have been targeted by several groups as proposed structural models of the OEC as evidence has emerged that it contained a mixed Mn–Ca–oxido cluster[25–31]. Calcium–manganese clusters remain uncommon, although recently a number of such complexes have been isolated and structurally characterized[9,21,26–31]. Because heterometallic clusters are often synthesized by self-assembly, controlling the composition and relative arrangement of metals has been a challenge. Furthermore, these synthetic protocols are not necessarily extended easily to the incorporation of other redox-inactive metals instead of calcium. To develop general syntheses of heterometallic clusters, we used a multinucleating ligand that affords versatile trimetallic (M^{II}_3) precursors[23]. These Mn^{II}_3 species could be elaborated to site-differentiated tetramanganese cubanes, Mn_4O_4, as well as to heteronuclear Mn_3CaO_4 clusters[21]. Strategies for general synthetic protocols to related heteronuclear complexes were then explored.

A dicationic calcium-bridged hexamanganese complex ($[LMn^{III}_2Mn^{II}O(OAc)_3]_2Ca(OTf)_2$) in which each trimanganese unit is coordinated by a μ_3-oxide was prepared and proposed to be an intermediate in the synthesis of $LMn^{IV}_3CaO_4(OAc)_3(THF)$[21]. In an effort to isolate other manganese clusters of high oxidation state relevant for the preparation of structural mimics of the OEC, $[LMn^{III}_2Mn^{II}O(OAc)_3]_2Ca(OTf)_2$ was treated with $Ca(OTf)_2$ and PhIO in 1,2-dimethoxyethane (DME) to form a red-purple

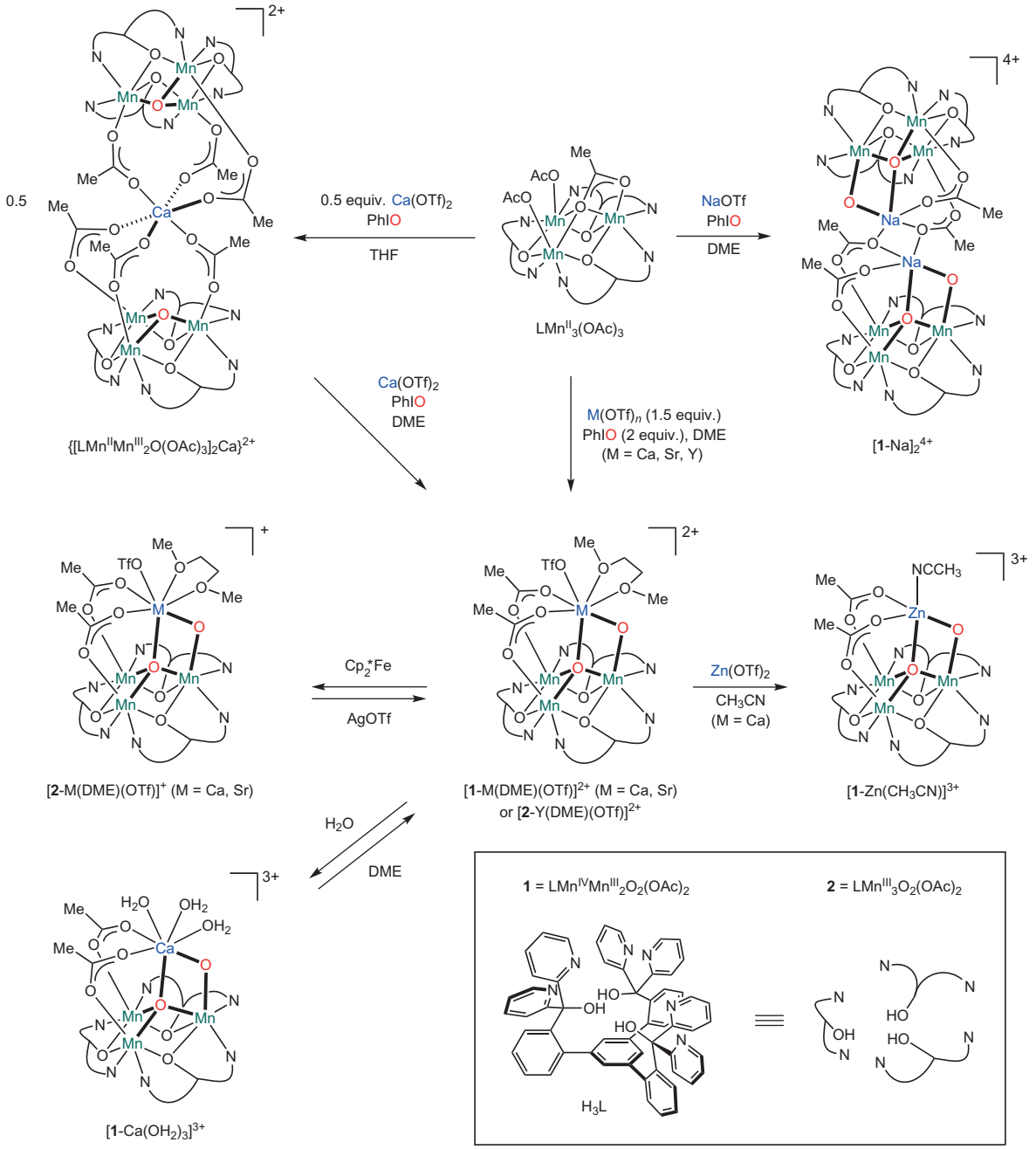

Figure 2 | Synthesis of tetrametallic trimanganese dioxido complexes. The reduced precursor $LMn_3(OAc)_3$ was oxidized in the presence of metal triflate salts to form $[LMn_3MO_2(OAc)_2]$ compounds (M=Na, Ca, Sr, Y). Complex [**1**-Ca(DME)(OTf)]$^{2+}$ (**1** = $LMn^{IV}Mn^{III}_2O_2(OAc)_2$) undergoes reversible chemical reduction, substitution of Zn^{2+} for Ca^{2+}, or exchange of the DME ligand for coordinated water molecules.

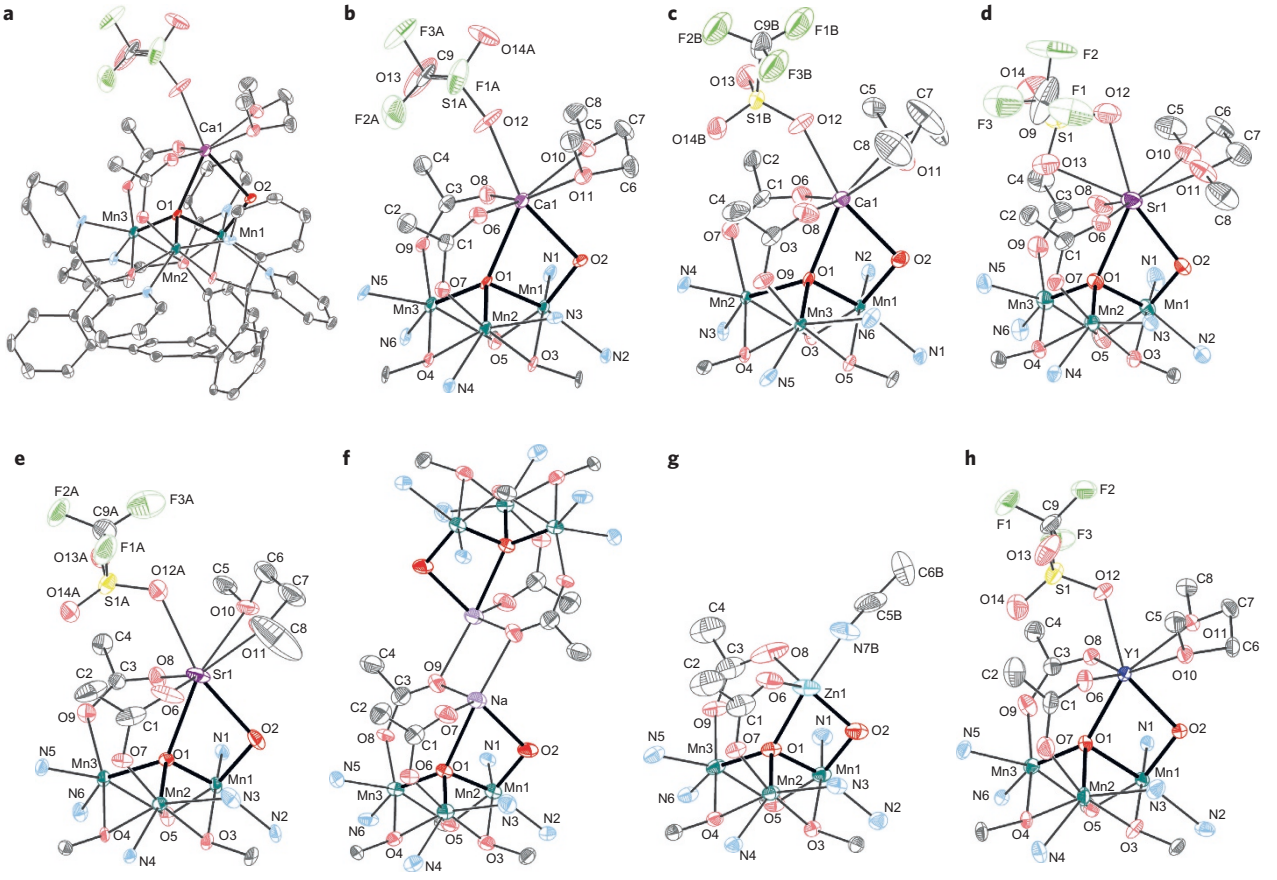

Figure 3 | Solid-state structures of reported complexes (thermal ellipsoids shown at 50% level). Hydrogen atoms and outer-sphere anions not shown for clarity. **a**, Full structure of [**1**-Ca(DME)(OTf)][OTf]$_2$. **b**, Truncated view of [**1**-Ca(DME)(OTf)][OTf]$_2$. **c**, Truncated view of [**2**-Ca(DME)(OTf)][OTf]. **d**, Truncated view of [**1**-Sr(DME)(OTf)][OTf]$_2$. **e**, Truncated view of [**2**-Sr(DME)(OTf)][OTf]. **f**, Truncated view of [**1**-Na]$_2$[OTf]$_4$. **g**, Truncated view of [**1**-Zn(CH_3CN)][OTf]$_3$. **h**, Truncated view of [**2**-Y(DME)(OTf)][OTf]$_2$.

compound (Fig. 2). The same compound was also independently synthesized in high yield (84%) in one step from the more reduced $LMn^{II}_3(OAc)_3$ precursor (Fig. 2). A single-crystal X-ray diffraction (XRD) study of this species confirmed the material to be a calcium trimanganese dioxo complex ($[\mathbf{1}\text{–Ca(DME)(OTf)}]^{2+}$ ($\mathbf{1} = LMn^{IV}Mn^{III}_2O_2(OAc)_2$), Fig. 3). The metal oxidation states were assigned based on crystallographic, X-ray absorption spectroscopy (XAS) and magnetism data (vide infra). In this complex, as in $LMn^{II}_3(OAc)_3$, the three manganese centres are bridged by three alkoxide donors from L, forming a six-membered ring, and the pyridine nitrogens of each dipyridyloxymethyl moiety coordinate to adjacent metal centres. Ca^{2+} is bridged to the trimanganese cluster by a μ_4-oxido, to the Mn^{IV} centre by a μ_2-oxido, and to the remaining Mn^{III} centres by bridging acetate moieties. The Ca^{2+} is further coordinated by a bidentate DME ligand and a trifluoromethanesulfonate anion. Two trifluoromethanesulfonate ions remain outer-sphere. The isolated compounds reported here display diagnostic ^{1}H NMR spectra, although the paramagnetically broadened and shifted signals have not been assigned. The addition of excess water to a CD_2Cl_2 solution of $[\mathbf{1}\text{–Ca(DME)(OTf)}]^{2+}$ forms a new species by ^{1}H NMR spectroscopy (Supplementary Fig. S2) that was identified by XRD as the tris(aqua) complex $[\mathbf{1}\text{–Ca(OH}_2)_3]^{3+}$ (Supplementary Fig. S26). Addition of DME to the CD_2Cl_2 solution of $[\mathbf{1}\text{–Ca(OH}_2)_3]^{3+}$ converts the complex back to $[\mathbf{1}\text{–Ca(DME)(OTf)}]^{2+}$ (^{1}H NMR spectroscopy, Supplementary Fig. S9). In the solid state, $[\mathbf{1}\text{–Ca(DME)(OTf)}]^{2+}$ is stable for weeks under ambient conditions.

Treatment of a DME suspension of $[\mathbf{1}\text{–Ca(DME)(OTf)}]^{2+}$ with the one-electron reductant decamethylferrocene yields the singly reduced product $[\mathbf{2}\text{–Ca(DME)(OTf)}]^{+}$ ($\mathbf{2} = LMn^{III}_3O_2(OAc)_2$). The chemical reversibility of this conversion is demonstrated by treatment of $[\mathbf{2}\text{–Ca(DME)(OTf)}]^{+}$ with AgOTf to convert back to $[\mathbf{1}\text{–Ca(DME)(OTf)}]^{2+}$. ^{1}H NMR analysis is consistent with clean interconversion of these two clusters. An XRD study of $[\mathbf{2}\text{–Ca(DME)(OTf)}]^{+}$ reveals a cluster isostructural to $[\mathbf{1}\text{–Ca(DME)(OTf)}]^{2+}$ with only slight bond distance changes (see below), indicating little rearrangement of the cluster upon reduction.

The variable-temperature magnetic susceptibilites of $[\mathbf{1}\text{–Ca(DME)(OTf)}][OTf]_2$ and $[\mathbf{2}\text{–Ca(DME)(OTf)}][OTf]$ were studied (Supplementary Fig. S11). For $[\mathbf{1}\text{–Ca(DME)(OTf)}][OTf]_2$, dominant ferromagnetic coupling between Mn ions is observed (see Supplementary Table S1 for fitting parameters). At 14 K, the $\chi_M T$ value (χ_M = molar magnetic susceptibility) increases to a maximum of 18.7 cm^3 mol^{-1} K, which is close to the expected spin-only value of an $S = 11/2$ system (17.9 cm^3 mol^{-1} K, $g = 2$ (g is the effective gyromagnetic ratio)). Different values would be expected for a more oxidized $S = 5$ system (15 cm^3 mol^{-1} K, $g = 2$) or a more reduced $S = 6$ system (21 cm^3 mol^{-1} K, $g = 2$). These results support the oxidation state assignment of $[\mathbf{1}\text{–Ca(DME)(OTf)}]^{2+}$ as $Mn^{IV}Mn^{III}_2$. The $\chi_M T$ value of $[\mathbf{2}\text{–Ca(DME)(OTf)}][OTf]$ approaches 10.2 cm^3 mol^{-1} K at 300 K, which is near the expected spin-only value of three uncoupled Mn^{III} ions ($S = 2$ spins, 3 cm^3 mol^{-1} K, $g = 2$). The $\chi_M T$ value decreases at low temperatures, reaching 2.6 cm^3 mol^{-1} K at 4 K, which shows a dominant antiferromagnetic interaction (Supplementary Table S1). To further confirm the oxidation state assignment of the isolated species, Mn X-ray absorption near edge spectra (XANES) were collected for $[\mathbf{1}\text{–Ca(DME)(OTf)}](OTf)_2$ and $[\mathbf{2}\text{–Ca(DME)(OTf)}](OTf)$ (Fig. 4a).

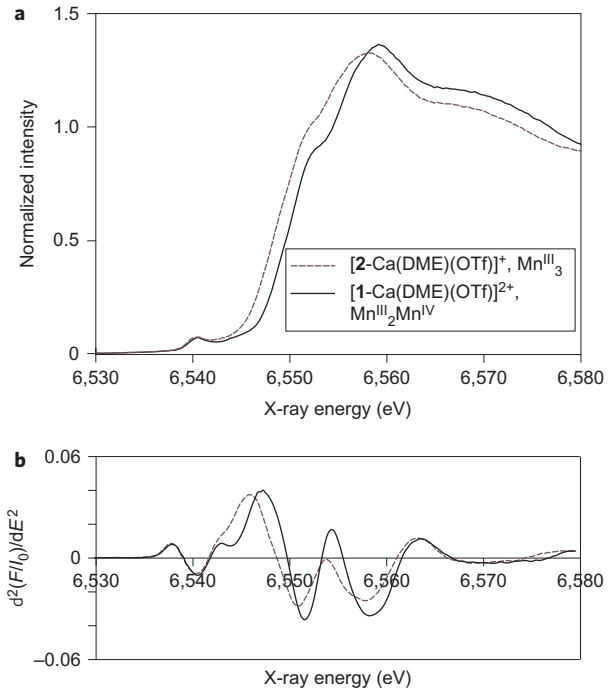

Figure 4 | The shift in the rising edge energy in the Mn XANES spectra. The shift for [**1**–Ca(DME)(OTf)][OTf]$_2$ (solid line) and [**2**–Ca(DME)(OTf)][OTf] (dashed line) (6,549.76 and 6,548.66 eV, respectively) suggests a one-electron oxidation state change. **a**,**b**, Mn XANES spectra (**a**) and second derivative spectra (**b**).

The rising edge energy, taken as a zero crossing point of the second derivative spectrum (Fig. 4b), is shifted to a higher energy by ~1.0 eV from [**2**–Ca(DME)(OTf)](OTf) (6,548.66 eV) to [**1**–Ca(DME)(OTf)](OTf)$_2$ (6,549.76 eV). Such an edge shift is consistent with a one-electron oxidation state change in redox-active Mn complexes[32], when the geometry and type of ligands are highly conserved. This result, correlated with charge balance in the solid-state structure, magnetism and chemical reactivity, therefore supports the formal oxidation state assignments for [**1**–Ca(DME)(OTf)](OTf)$_2$ and [**2**–Ca(DME)(OTf)](OTf) as $Mn^{IV}Mn^{III}_2$ and Mn^{III}_3 respectively.

To study the effects of the redox-inactive centre on the properties of the [Mn_3O_2] core, the analogous Sr^{2+}-, Y^{3+}-, Na^+- and Zn^{2+}-capped trimanganese dioxo complexes were targeted (Figs 2 and 3). Treatment of $LMn^{II}_3(OAc)_3$ with PhIO and $M(OTf)_n$ (M = Na, Sr, Y) led to new species with ^{1}H NMR spectroscopic characteristics similar to compounds [**1**–Ca(DME)(OTf)]$^{2+}$ and [**2**–Ca(DME)(OTf)]$^+$. Complexes [**1**–Sr(DME)(OTf)]$^{2+}$ and [**2**–Y(DME)(OTf)]$^{2+}$ are structurally analogous to [**1**–Ca(DME)(OTf)]$^{2+}$, with the redox-inactive metal bridged by two oxido moieties to the trimanganese cluster and further coordinated by a DME molecule and a triflate anion (Fig. 3d,h). The yttrium-capped dioxo compound was isolated in the more reduced Mn^{III}_3 state rather than the $Mn^{IV}Mn^{III}_2$ state observed under the same reaction conditions for the calcium and strontium dioxo compounds. Similar to the reduction of [**1**–Ca(DME)(OTf)]$^{2+}$ to [**2**–Ca(DME)(OTf)]$^+$, the reduced strontium compound [**2**–Sr(DME)(OTf)]$^+$ was prepared by treating [**1**–Sr(DME)(OTf)]$^{2+}$ with decamethylferrocene. The Na-capped dioxo complex [**1**–Na]$_2^{4+}$ was isolated in the solid state as a dimer of Mn_3NaO_2 moieties via acetate bridges. Each Mn_3NaO_2 core is structurally similar to the Ca^{2+}, Sr^{2+} and Y^{3+} analogues, with the Na^+ cation bridged by two oxidos to the trimanganese moiety (Fig. 3f). Preparation of the Zn-capped compound [**1**–Zn(CH_3CN)]$^{3+}$was accomplished by the addition of $Zn(OTf)_2$ to a CH_3CN solution of [**1**–Ca(DME)(OTf)]$^{2+}$, leading to substitution of Ca^{2+} with Zn^{2+}. An XRD study of [**1**–Zn(CH_3CN)]$^{3+}$ grown from an acetonitrile/diethyl ether mixture shows one acetonitrile coordinated to the Zn^{2+} centre. The Mn_3ZnO_2 core is structurally similar to the other Mn_3MO_2 moieties reported here. The magnetic susceptibilities of the $Mn^{IV}Mn^{III}_2$ complexes [**1**–Sr(DME)(OTf)][OTf]$_2$, [**1**–Na]$_2$[OTf]$_4$ and [**1**–Zn(CH_3CN)][OTf]$_3$ were measured, and all demonstrate ferromagnetic coupling of spins close to that of [**1**–Ca(DME)(OTf)][OTf]$_2$, supporting the same formal oxidation state assignment (Supplementary Fig. S11).

Analysis of the solid-state structures show that the distances from the redox-inactive metals to the bridging oxido moieties vary as expected based on the ionic radius of the ion M, with the M—O distances increasing from [**1**–Zn(CH_3CN)]$^{3+}$ (2.008(3), 2.090(3) Å) to [**1**–Sr(DME)(OTf)]$^{2+}$ (2.510(5), 2.651(4) Å) (Table 1). Upon reduction of the $Mn^{IV}Mn^{III}_2$ clusters [**1**–Ca(DME)(OTf)]$^{2+}$ and [**1**–Sr(DME)(OTf)]$^{2+}$ to form the Mn^{III}_3 complexes [**2**–Ca(DME)(OTf)]$^+$ and [**2**–Sr(DME)(OTf)]$^+$, the M–(μ_4-O) distances contract, indicating a stronger interaction with the redox-inactive metal as the interaction of the μ_4-oxido with the trimanganese core weakens due to increased population of σ-antibonding orbitals in d^4, Mn^{III} centres. As expected, the Mn—O distances increase upon reduction (compounds **2** versus **1**), but only small variations are observed based upon the redox-inactive metal. [**2**–Y(DME)(OTf)]$^{2+}$ displays the longest Mn–oxido average distance, consistent with the yttrium centre, the most Lewis-acidic metal of the series, drawing more electron density from the oxido moieties and weakening the Mn—O interactions. Notably, the bond distances of the Mn_3O_2 core are essentially the same in

Table 1 | Selected bond lengths (in Å) for reported complexes.

	[1-Ca(DME)(OTf)]$^{2+}$	[2-Ca(DME)(OTf)]$^+$	[1-Sr(DME)(OTf)]$^{2+}$	[2-Sr(DME)(OTf)]$^+$	[1-Na]$_2^{4+}$	[1-Zn(CH_3CN)]$^{3+}$	[2-Y(DME)(OTf)]$^{2+}$
M-Mn1	3.317(1)	3.283(1)	3.476(1)	3.424(1)	3.216(3)	3.0005(8)	3.3011(6)
M-Mn2	3.749(1)	3.802(1)	4.005(1)	3.923(1)	3.739(3)	3.3495(9)	3.7533(6)
M-Mn3	4.042(1)	4.034(1)	4.149(1)	4.166(1)	3.942(3)	3.7595(9)	3.8592(6)
Mn1-Mn2	3.0480(9)	3.0111(9)	3.062(1)	3.020(2)	3.076(2)	3.065(1)	3.2110(7)
Mn1-Mn3	3.0486(9)	3.1537(9)	3.051(1)	3.142(2)	3.000(2)	3.038(1)	3.0494(7)
Mn2-Mn3	3.0179(9)	3.0541(9)	3.025(1)	3.064(2)	3.004(2)	3.0739(9)	3.1223(7)
M-O2	2.349(3)	2.368(3)	2.510(5)	2.508(5)	2.300(6)	2.008(3)	2.269(2)
M-O1	2.452(3)	2.397(3)	2.651(4)	2.536(5)	2.422(6)	2.090(3)	2.232(2)
Mn1-O2	1.842(3)	1.887(3)	1.841(4)	1.869(5)	1.840(5)	1.862(3)	1.889(2)
Mn1-O1	2.017(3)	1.939(3)	2.022(4)	1.943(5)	1.995(5)	1.981(3)	2.150(2)
Mn2-O1	1.913(3)	2.159(3)	1.932(4)	1.856(5)	1.936(5)	1.946(3)	2.177(2)
Mn3-O1	1.958(3)	1.860(3)	1.936(4)	2.172(5)	1.889(5)	1.960(3)	1.895(2)
Avg. Mn-O1	1.96	1.99	1.96	1.99	1.94	1.96	2.07

The Mn–O bond lengths vary depending on manganese oxidation state, but not significantly due to the redox-inactive metal M. M–O bond lengths vary with ionic radius. All estimated standard deviations were calculated rigorously from the full covariance matrix[42].

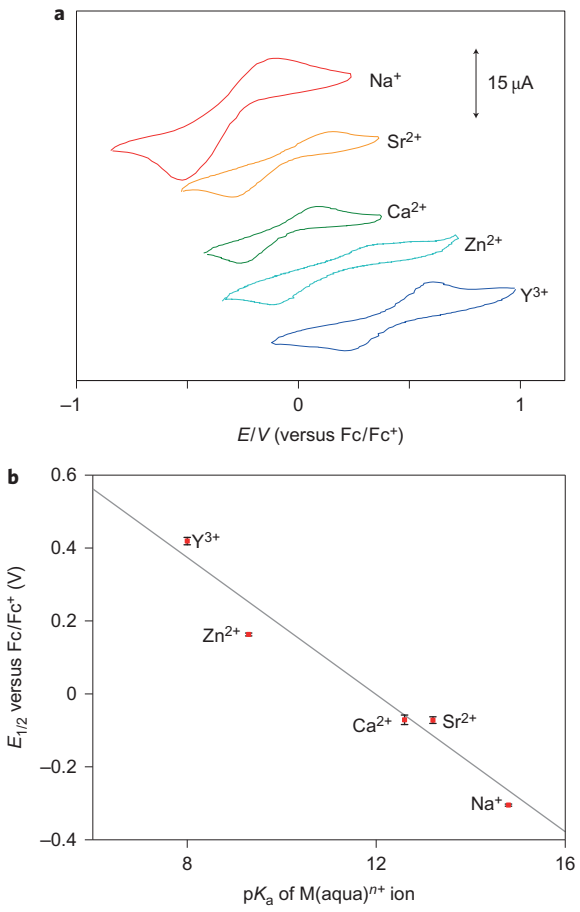

Figure 5 | The redox potentials of the [MMn_3O_2] complexes are correlated with the Lewis acidity of the redox-inactive metal. a, CVs of reported complexes in 0.1 M NBu_4PF_6 10:1 CH_2Cl_2/DME (CV of [**1**-Na]$_2^{4+}$ in CH_2Cl_2) using a glassy carbon disc electrode at a scan rate of 100 mV s^{-1}. **b**, Dependence of $E_{1/2}$ of $Mn^{IV}Mn^{III}{}_2/Mn^{III}{}_3$ couple on pK_a of M(aqua)$^{n+}$ ion[36]. Error bars correspond to the standard deviation of the reduction potentials measured from three independent samples.

[**1**–Ca(DME)(OTf)]$^{2+}$ and [**1**–Sr(DME)(OTf)]$^{2+}$. These observations are consistent with XAS studies of Sr-substituted PSII, indicating no significant structural change in the OEC from Ca-substituted PSII[3,33].

We and others have reported studies that suggest a significant effect of redox-inactive metals on the electron transfer properties of metal–oxido species, a phenomenon of particular relevance in biological systems and heterogeneous mixed metal oxides[7,8,15,21,24,34–36]. With a series of well-defined and structurally analogous Mn_3MO_2 complexes in hand, we investigated the effect of metal M on the reduction potential of the clusters. The cyclic voltammogram (CV) of a 10:1 CH_2Cl_2/DME solution of [**1**–Ca(DME)(OTf)]$^{2+}$ (0.1 M NBu_4PF_6) shows two quasireversible redox couples at −70 and −530 mV versus the ferrocene/ferrocenium couple (Fc/Fc^+) (Supplementary Fig. S15). Because [**1**–Ca(DME)(OTf)]$^{2+}$ is chemically reduced to [**2**–Ca(DME)(OTf)]$^+$ by the addition of 1 equiv. of decamethylferrocene ($E^O \approx -0.48$ V versus Fc/Fc^+ in CH_2Cl_2), the couple centred at −70 mV is assigned as the $[Mn^{IV}Mn^{III}{}_2/Mn^{III}{}_3]$ couple. A 10:1 CH_2Cl_2/DME solution of [**1**–Ca(DME)(OTf)]$^{2+}$ (0.05 M LiOTf electrolyte) was electrolysed at a potential of −0.25 V versus Ag/Ag^+ to form a new species by ^{1}H NMR spectroscopy. The amount of current passed at that potential supports the assignment of the wave at −70 mV as the one-electron reduction of [**1**–Ca(DME)(OTf)]$^{2+}$. Independently prepared [**2**–Ca(DME)(OTf)]$^+$ reacts with excess LiOTf to cleanly form a product whose ^{1}H NMR spectrum matches that of the controlled potential electrolysis product described above (Supplementary Fig. S13). Under the same conditions, [**1**–Ca(DME)(OTf)]$^{2+}$ does not react with LiOTf. The more negative redox couple at −530 mV is presumed to correspond to the $[Mn^{III}{}_3/Mn^{III}{}_2Mn^{II}]$ couple, but the more reduced product has not yet been isolated.

As the electrochemical studies are presumed to be of intact clusters, the solution stability of the [MMn_3O_2] core was studied. Isotopically labelled $LCaMn_3{}^{18}O_2(OAc)_2(DME)(OTf)_3$ ([**1***–Ca(DME)(OTf)][OTf]$_2$) was prepared and mixed with 1 equiv. of natural abundance [**1**–Ca(DME)(OTf)]$^{2+}$ in dichloromethane at room temperature, and the mixture was analysed over time using electrospray ionization mass spectrometry (ESI-MS). Less than 20% isotopic scrambling occurs on the timescale of the electrochemical experiments (∼18% after 1 h at room temperature). Additionally, methylene chloride solutions of [**1**–Ca(DME)(OTf)]$^{2+}$ are stable at room temperature under anhydrous conditions for days (^{1}H NMR spectroscopy). The addition of 10 equiv. of $Ca(OTf)_2$ to the solution of [**1**–Ca(DME)(OTf)]$^{2+}$ does not change the reduction potential of the complex (Supplementary Fig. S17), indicating that any equilibrium towards dissociation of the clusters lies towards Ca^{2+} association. To interrogate the effect of the Ca-coordinated ligands, under the same conditions, the reduction of [**1**–Ca(OH$_2$)$_3$]$^{3+}$ occurs within 30 mV of that of [**1**–Ca(DME)(OTf)]$^{2+}$ (Supplementary Fig. S16), suggesting that the capping ligands on the Ca^{2+} centre do not significantly affect the reduction potentials of the clusters.

The CVs of [**1**–Sr(DME)(OTf)]$^{2+}$, [**2**–Y(DME)(OTf)]$^{2+}$, [**1**–Zn(CH$_3$CN)]$^{3+}$ and [**1**–Na]$_2^{4+}$ all display the $[Mn^{IV}Mn^{III}{}_2/Mn^{III}{}_3]$ couple observed for [**1**–Ca(DME)(OTf)]$^{2+}$, although at different potentials (Fig. 5a). Although the peak-to-peak separations of the observed couples are large when measured at a glassy carbon electrode ($\Delta E_p \approx 400$ mV), indicating slow electron transfer to the complexes, the $E_{1/2}$ values calculated from the CVs of [**1**–Ca(DME)(OTf)]$^{2+}$, [**1**–Sr(DME)(OTf)]$^{2+}$ and [**1**–Na]$_2^{4+}$ are in good agreement with CVs collected using a hanging drop mercury electrode, with $\Delta E_p \approx 200$ mV (Supplementary Fig. S14). The $E_{1/2}$ corresponding to the reduction of [**1**–Ca(DME)(OTf)]$^{2+}$ to [**2**–Ca(DME)(OTf)]$^+$ was also measured by monitoring the electronic absorption spectrum upon titration with dimethylferrocene (Supplementary Fig. S18), and the calculated values (−0.1 V versus Fc/Fc^+) are close to the value from the CV (−0.07 V versus Fc/Fc^+).

As structural characterization was obtained only for clusters displaying the $Mn^{IV}Mn^{III}{}_2$ and $Mn^{III}{}_3$ oxidation states, these are the reduction potentials that are compared below. Moreover, the more highly oxidized species are pertinent to the moieties present in the OEC and proposed for water oxidation catalysts. The $E_{1/2}$ values of the $[Mn^{IV}Mn^{III}{}_2/Mn^{III}{}_3]$ couple become more positive as the charge of the redox-inactive metal increases. This trend suggests that the increased charge of the proximal redox-inactive cation facilitates reduction of the manganese centres. The $E_{1/2}$ value for the Zn^{2+} complex appears at potentials ∼230 mV more positive compared to the Ca^{2+} and Sr^{2+} species. Although [**1**–Zn(CH$_3$CN)]$^{3+}$ is tricationic and [**1**–Ca(DME)(OTf)]$^{2+}$ and [**1**–Sr(DME)(OTf)]$^+$ are dicationic, the $E_{1/2}$ of the $[Mn^{IV}Mn^{III}{}_2/Mn^{III}{}_3]$ couple of [**1**–Ca(OH$_2$)]$^{3+}$, also a tricationic complex, is more positive than that of [**1**–Ca(DME)(OTf)]$^{2+}$, by less than 30 mV. The more positive potential of the Zn^{2+} compound is inconsistent with a purely electrostatic explanation of the change in reduction potentials, as proposed for oxo-bridged manganese dimers with alkali and alkali earth metal ions associated via salen ligands modified with crown ether moieties[35].

The effect of redox-inactive metals on the kinetics of electron transfer to a non-haem $Fe^{IV}O$ species has been linked previously to the Lewis acidity of the metal[8,37]. The $E_{1/2}$ values of the

$[Mn^{IV}Mn^{III}{}_2/Mn^{III}{}_3]$ couples measured above in organic solvents were plotted against the pK_a of the metal aqua ions, $M(aqua)^{n+}$, in water[38], used here as a measure of the Lewis acidity of the metal M. A remarkable linear correlation is observed (Fig. 5b) that clearly links the effect of the redox-inactive metal to the cluster reduction potential in terms of the Lewis acidity of the metal. The slope provides a quantitative measure of this correlation, with each pK_a unit shifting the potential by ~100 mV. This effect is probably a consequence of the interaction between the oxido moieties and redox-inactive metals versus manganese centres. The stronger Lewis acid is expected to draw more electron density from the oxido ligands and to destabilize the higher-oxidation-state manganese centres.

The above findings have implications for biological and heterogeneous metal catalysts for water oxidation and other redox processes. Catalysis occurs at discrete multinuclear sites, consisting of five metal centres for the OEC in PSII and fewer than ten metal centres for heterogeneous manganese and cobalt oxides. The potential of the cluster is expected to vary based on structure and number of oxido ligands. For example, the reduction potential of the $[Mn^{IV}Mn^{III}{}_2CaO_2/Mn^{III}{}_3CaO_2]$ couple reported here is more positive than that of the $[Mn^{IV}{}_3CaO_4/Mn^{IV}{}_2Mn^{III}CaO_4]$ couple of the $CaMn_3$ cubane cluster[21], despite the higher manganese oxidation states in the latter complex, probably due to the greater number of oxido ligands. Changing the nature of the redox-inactive metal component of the cluster, without a structural change of the cluster, allows for drastic variation of the reduction potential in both directions, potentially from values that render the chemistry of interest (for example, water oxidation) thermodynamically unfavourable to values that make it favourable. Tuning of the reduction potentials of mixed metal-oxide clusters by Lewis acids is an appealing strategy for designing practical catalysts for water splitting.

It is notable in the present series that the Ca^{2+} and Sr^{2+} variants have essentially the same potentials, which is consistent with the observation that substitution of Sr^{2+} for Ca^{2+} in PSII retains reactivity and a similar electronic structure[33,39]. Although a previously proposed role of the Ca^{2+} (or Sr^{2+}) of the OEC in facilitating the attack of a water or hydroxide moiety on an electrophilic manganese oxo is still possible[40], the reported results support a significant role in redox tuning of the cluster.

In summary, a series of tetrametallic dioxo complexes containing redox-inactive metal ions in the +1 to +3 oxidation states were synthesized using a trinucleating ligand framework. The structural characteristics of these complexes, with the oxido ligands bridging the redox-inactive metals and the manganese centres, make them particularly relevant to biological and heterogeneous metal–oxido clusters. Electrochemical studies of these compounds show that the reduction potentials are highly dependent upon the Lewis acidity of the redox-inactive metal, identifying the chemical basis for the observed differences in electrochemistry. This correlation provides evidence for the role of the Ca^{2+} ion in modulating the redox potential of the OEC and of other redox-inactive ions in tuning the redox potentials of other metal-oxide electrocatalysts. The observed linear dependence between cluster potential and Lewis acidity provides a rational strategy for tuning the redox properties of heterometallic metal–oxido clusters of interest for catalysis. Current studies are focused on further understanding the relationship between the structures of mixed-metal manganese–oxido clusters and their reactivity.

Methods

Unless indicated otherwise, reactions were carried out in oven-dried glassware in a glovebox under a nitrogen atmosphere. Anhydrous tetrahydrofuran (THF) was purchased from Aldrich in 18-litre Pure-Pac containers. Anhydrous dichloromethane, diethyl ether and THF were purified by sparging with nitrogen for 15 min and then passing under nitrogen pressure through a column of activated A2 alumina. Anhydrous DME was dried over sodium/benzophenone ketyl and vacuum-transferred onto molecular sieves. CD_2Cl_2 was purchased from Cambridge Isotope Laboratories, dried over calcium hydride, then degassed by three freeze–pump–thaw cycles and vacuum-transferred before use.

Iodosobenzene was prepared according to literature procedures[41]. $LMn_3(OAc)_3$ and $[LMn_3O(OAc)_3]_2Ca(OTf)_2$ were prepared according to previously published procedures[21,23]. (Caution! Iodosobenzene is potentially explosive and should be used only in small quantities.)

The syntheses of all reported compounds, characterization methods and equipment are described in the Supplementary Information.

Synthesis of [1–Ca(DME)(OTf)][OTf]$_2$. In the glovebox, a round-bottom flask equipped with a stir bar was charged with $LMn_3(OAc)_3$ (2.0 g, 1.67 mmol) and $Ca(OTf)_2$ (0.90 g, 2.67 mmol, 1.6 equiv.). DME (200 ml) was added, and the yellow suspension was stirred at room temperature for 5 min. Iodosobenzene (0.81 g, 3.68 mmol, 2.2 equiv.) was added as a solid, and the mixture was stirred at room temperature for 4 h, turning from yellow to purple. The purple solid was collected via filtration, washed with DME, then extracted with dichloromethane. The red-purple solution was concentrated *in vacuo* to yield the product as a red-purple solid (2.45 g, 84%). ^{1}H NMR (CD_2Cl_2, 300 MHz): δ 77.8, 76.5, 72.3, 69.6, 60.5, 53.7, 48.4, 38.6, 37.0, 24.2, 19.9, 17.5, 15.9, 8.1, 3.3, 2.9, −19.3, −23.5, −24.9, −26.4, −29.1 ppm. ^{19}F NMR (CD_2Cl_2): δ −74.4 ppm. UV-Vis (CH_2Cl_2, λ_{max} (ε)): 498 (1,410 M^{-1} cm^{-1}), 846 (640 M^{-1} cm^{-1}) nm. Anal. Calcd. For $C_{68}H_{55}CaF_9Mn_3N_6O_{20}S_3$: C, 46.72; H, 3.17; N, 4.81. Found: C, 46.92; H, 3.27; N, 4.89.

Synthesis of [2–Ca(DME)(OTf)][OTf]. In the glovebox, a round-bottom flask equipped with a stir bar was charged with $[\mathbf{1}–Ca(DME)(OTf)]^{2+}$ (0.750 g, 0.429 mmol) and decamethylferrocene (0.140 g, 0.429 mmol, 1 equiv.). DME (30 ml) was added, and the purple mixture was stirred at room temperature for 1 h. The grey-purple precipitate was collected on a fritted glass funnel and washed with DME, then extracted with cold THF (40 ml). The purple filtrate was concentrated to ~20 ml *in vacuo*, then cooled to −35 °C to precipitate out more $Cp^*{}_2Fe^+$, which was filtered off over Celite. The purple filtrate was concentrated *in vacuo* to a purple solid, then recrystallized from DME/CH_2Cl_2/hexanes to yield the product as a purple solid (0.405 g, 59%). ^{1}H NMR (CD_2Cl_2, 300 MHz): δ 65.1, 57.8, 50.7, 41.6, 35.3, 29.6, 15.7, 15.0, 14.2, 8.2, 3.0, −9.6, −12.6, −17.0, −17.9 ppm. ^{19}F NMR (CD_2Cl_2): δ −74.6 ppm. UV-Vis (CH_2Cl_2, λ_{max} (ε)): 495 (710 M^{-1} cm^{-1}), 860 (310 M^{-1} cm^{-1}) nm. Anal. Calcd. for $C_{67}H_{55}CaF_6Mn_3N_6O_{17}S_2$: C, 50.32; H, 3.47; N, 5.26. Found: C, 50.04; H, 3.63; N, 5.06.

Electrochemistry. Electrochemical measurements were recorded using a Pine Instrument Company AFCBP1 bipotentiostat using the AfterMath software package. CVs were recorded on ~1 mM solutions of the relevant complexes in the glovebox, at 20 °C, with an auxiliary Pt-coil electrode, a Ag/Ag+ reference electrode (0.01 M $AgNO_3$, 0.1 M ^{n}Bu$_4$NPF$_6$ in CH_3CN) and a 3.0 mm glassy carbon electrode disc (BASI). The electrolyte solutions were 0.1 M ^{n}Bu$_4$NPF$_6$ in CH_2Cl_2 ($[\mathbf{1}–Na]_2^{4+}$) or 10:1 CH_2Cl_2/DME ($[\mathbf{1}–Ca(DME)(OTf)]^{2+}$, $[\mathbf{1}–Sr(DME)(OTf)]^{2+}$, $[\mathbf{1}–Zn(CH_3CN)]^{3+}$ and $[\mathbf{2}–Y(DME)(OTf)]^{2+}$). For $[\mathbf{1}–Ca(DME)(OTf)]^{2+}$, $[\mathbf{1}–Sr(DME)(OTf)]^{2+}$ and $[\mathbf{1}–Na]_2^{4+}$, CVs were also recorded in an electrolyte solution of 0.1 M ^{n}Bu$_4$NPF$_6$ in CH_2Cl_2 using a hanging mercury drop electrode (BASI CGME). Using the average mass of the mercury drop (0.037 g), the surface area of the drop (assumed to be a sphere) was calculated to be 0.095 cm^2. All reported values are referenced to an internal Fc/Fc^+ couple.

Received 29 August 2012; accepted 22 January 2013; published online 3 March 2013

References

1. Fukuzumi, S. & Ohkubo, K. Metal ion-coupled and decoupled electron transfer. *Coord. Chem. Rev.* **254,** 372–385 (2010).
2. Fukuzumi, S. in *Progress in Inorganic Chemistry* **Vol. 56** (ed. Karlin, K. A.) 49–154 (Wiley, 2009).
3. Yachandra, V. K. & Yano, J. Calcium in the oxygen-evolving complex: structural and mechanistic role determined by X-ray spectroscopy. *J. Photochem. Photobiol. B* **104,** 51–59 (2011).
4. Yocum, C. F. The calcium and chloride requirements of the O_2 evolving complex. *Coord. Chem. Rev.* **252,** 296–305 (2008).
5. McEvoy, J. P. & Brudvig, G. W. Water-splitting chemistry of photosystem II. *Chem. Rev.* **106,** 4455–4483 (2006).
6. Park, J. *et al.* Scandium ion-enhanced oxidative dimerization and *N*-demethylation of *N*,*N*-dimethylanilines by a non-heme iron(IV)–oxo complex. *Inorg. Chem.* **50,** 11612–11622 (2011).
7. Fukuzumi, S. *et al.* Crystal structure of a metal ion-bound oxoiron(IV) complex and implications for biological electron transfer. *Nature Chem.* **2,** 756–759 (2010).
8. Morimoto, Y. *et al.* Metal ion-coupled electron transfer of a nonheme oxoiron(IV) complex: remarkable enhancement of electron-transfer rates by Sc^{3+}. *J. Am. Chem. Soc.* **133,** 403–405 (2011).
9. Park, Y. J., Ziller, J. W. & Borovik, A. S. The effects of redox-inactive metal ions on the activation of dioxygen: isolation and characterization of a heterobimetallic complex containing a Mn^{III}-(μ-OH)-Ca^{II} core. *J. Am. Chem. Soc.* **133,** 9258–9261 (2011).

10. Park, Y. J. *et al.* Heterobimetallic complexes with M^{III}-(μ-OH)-M^{II} cores (M^{III}=Fe, Mn, Ga; M^{II}=Ca, Sr, and Ba): structural, kinetic, and redox properties. *Chem. Sci.* **4,** 717–726 (2013).
11. Miller, C. G. *et al.* A method for driving O-atom transfer: secondary ion binding to a tetraamide macrocyclic ligand. *J. Am. Chem. Soc.* **120,** 11540–11541 (1998).
12. Risch, M. *et al.* Water oxidation by electrodeposited cobalt oxides—role of anions and redox-inert cations in structure and function of the amorphous catalyst. *ChemSusChem* **5,** 542–549 (2012).
13. Kanan, M. W. *et al.* Structure and valency of a cobalt-phosphate water oxidation catalyst determined by *in situ* X-ray spectroscopy. *J. Am. Chem. Soc.* **132,** 13692–13701 (2010).
14. Kanan, M. W. & Nocera, D. G. *In situ* formation of an oxygen-evolving catalyst in neutral water containing phosphate and Co^{2+}. *Science* **321,** 1072–1075 (2008).
15. Wiechen, M., Zaharieva, I., Dau, H. & Kurz, P. Layered manganese oxides for water oxidation: alkaline earth cations influence catalytic activity in a photosystem II-like fashion. *Chem. Sci.* **3,** 2330–2339 (2012).
16. Najafpour, M. M., Ehrenberg, T., Wiechen, M. & Kurz, P. Calcium manganese(III) oxides ($CaMn_2O_4{\cdot}xH_2O$) as biomimetic oxygen-evolving catalysts. *Angew. Chem. Int. Ed.* **49,** 2233–2237 (2010).
17. Najafpour, M. M., Pashaei, B. & Nayeri, S. Calcium manganese(IV) oxides: biomimetic and efficient catalysts for water oxidation. *Dalton Trans.* **41,** 4799–4805 (2012).
18. Umena, Y., Kawakami, K., Shen, J. R. & Kamiya, N. Crystal structure of oxygen-evolving photosystem II at a resolution of 1.9 Å. *Nature* **473,** 55–U65 (2011).
19. Ferreira, K. N., Iverson, T. M., Maghlaoui, K., Barber, J. & Iwata, S. Architecture of the photosynthetic oxygen-evolving center. *Science* **303,** 1831–1838 (2004).
20. Yamada, Y., Yano, K., Hong, D. & Fukuzumi, S. $LaCoO_3$ acting as an efficient and robust catalyst for photocatalytic water oxidation with persulfate. *Phys. Chem. Chem. Phys.* **14,** 5753–5760 (2012).
21. Kanady, J. S., Tsui, E. Y., Day, M. W. & Agapie, T. A synthetic model of the Mn_3Ca subsite of the oxygen-evolving complex in photosystem II. *Science* **333,** 733–736 (2011).
22. Tsui, E. Y., Day, M. W. & Agapie, T. Trinucleating copper: synthesis and magnetostructural characterization of complexes supported by a hexapyridyl 1,3,5-triarylbenzene ligand. *Angew. Chem. Int. Ed.* **50,** 1668–1672 (2011).
23. Tsui, E. Y., Kanady, J. S., Day, M. W. & Agapie, T. Trinuclear first row transition metal complexes of a hexapyridyl, trialkoxy 1,3,5-triarylbenzene ligand. *Chem. Commun.* **47,** 4189–4191 (2011).
24. Kanady, J. S., Mendoza-Cortes, J. L., Tsui, E. Y., Nielsen, R. J., Goddard, W. A., and Agapie, T. Oxygen atom transfer and oxidative water incorporation in cuboidal Mn_3MO_n complexes based on synthetic, isotopic labeling, and computational studies. *J. Am. Chem. Soc.* **135,** 1073–1082 (2013).
25. Lacy, D. C., Park, Y. J., Ziller, J. W., Yano, J. & Borovik, A. S. Assembly and properties of heterobimetallic $Co^{II/III}/Ca^{II}$ complexes with aquo and hydroxo ligands. *J. Am. Chem. Soc.* **134,** 17526–17535 (2012).
26. Mukherjee, S. *et al.* Synthetic model of the asymmetric $[Mn_3CaO_4]$ cubane core of the oxygen-evolving complex of photosystem II. *Proc. Natl Acad. Sci. USA* **109,** 2257–2262 (2012).
27. Mishra, A. *et al.* Heteronuclear Mn–Ca/Sr complexes, and Ca/Sr EXAFS spectral comparisons with the oxygen-evolving complex of photosystem II. *Chem. Commun.* 1538–1540 (2007).
28. Mishra, A., Wernsdorfer, W., Abboud, K. A. & Christou, G. The first high oxidation state manganese-calcium cluster: relevance to the water oxidizing complex of photosynthesis. *Chem. Commun.* 54–56 (2005).
29. Kotzabasaki, V., Siczek, M., Lis, T. & Milios, C. J. The first heterometallic Mn–Ca cluster containing exclusively Mn(III) centers. *Inorg. Chem. Commun.* **14,** 213–216 (2011).
30. Hewitt, I. J. *et al.* A series of new structural models for the OEC in photosystem II. *Chem. Commun.* 2650–2652 (2006).
31. Nayak, S., Nayek, H. P., Dehnen, S., Powell, A. K. & Reedijk, J. Trigonal propeller-shaped $[Mn^{III}_3M^{II}Na]$ complexes (M=Mn, Ca): structural and functional models for the dioxygen evolving centre of PSII. *Dalton Trans.* **40,** 2699–2702 (2011).
32. Visser, H. *et al.* Mn K-edge XANES and Kβ XES studies of two Mn–Oxo binuclear complexes: investigation of three different oxidation states relevant to the oxygen-evolving complex of photosystem II. *J. Am. Chem. Soc.* **123,** 7031–7039 (2001).
33. Pushkar, Y., Yano, J., Sauer, K., Boussac, A., & Yachandra, V. K. Structural changes in the Mn_4Ca cluster and the mechanism of photosynthetic water splitting. *Proc. Natl Acad. Sci. USA* **105,** 1879–1884 (2008).
34. Leeladee, P. *et al.* Valence tautomerism in a high-valent manganese–oxo porphyrinoid complex induced by a Lewis acid. *J. Am. Chem. Soc.* **134,** 10397–10400 (2012).
35. Horwitz, C. P. & Ciringh, Y. Synthesis and electrochemical properties of oxo-bridged manganese dimers incorporating alkali and alkaline earth cations. *Inorg. Chim. Acta* **225,** 191–200 (1994).
36. Horwitz, C. P., Ciringh, Y. & Weintraub, S. T. Formation pathway of a Mn(IV),Mn(IV) bis(μ-oxo) dimer that incorporates alkali and alkaline earth cations and electron transfer properties of the dimer. *Inorg. Chim. Acta* **294,** 133–139 (1999).
37. Fukuzumi, S. & Ohkubo, K. Quantitative evaluation of Lewis acidity of metal ions derived from the *g* values of ESR spectra of superoxide: metal ion complexes in relation to the promoting effects in electron transfer reactions. *Chem. Eur. J.* **6,** 4532–4535 (2000).
38. Perrin, D. D. *Ionisation Constants of Inorganic Acids and Bases in Aqueous Solution* (Pergamon, 1982).
39. Cox, N. *et al.* Effect of Ca^{2+}/Sr^{2+} substitution on the electronic structure of the oxygen-evolving complex of photosystem II: a combined multifrequency EPR, ^{55}Mn-ENDOR, and DFT study of the S_2 state. *J. Am. Chem. Soc.* **133,** 3635–3648 (2011).
40. Pecoraro, V. L., Baldwin, M. J., Caudle, M. T., Hsieh, W. Y. & Law, N. A. A proposal for water oxidation in photosystem II. *Pure Appl. Chem.* **70,** 925–929 (1998).
41. Saltzman, H. & Sharefkin, J. G. Iodosobenzene. *Org. Synth. Coll.* **5,** 658–659 (1973).
42. Sheldrick, G. A short history of SHELX. *Acta Crysallogr. A* **64,** 112–122 (2008).
43. Symes, M. D., Surendranath, Y., Lutterman, D. A. & Nocera, D. G. Bidirectional and unidirectional PCET in a molecular model of a cobalt-based oxygen-evolving catalyst. *J. Am. Chem. Soc.* **133,** 5174–5177 (2011).
44. Yano, J. *et al.* Where water is oxidized to dioxygen: structure of the photosynthetic Mn_4Ca cluster. *Science* **314,** 821–825 (2006).
45. Peloquin, J. M. *et al.* ^{55}Mn ENDOR of the S_2-state multiline EPR signal of photosystem II: implications on the structure of the tetranuclear Mn cluster. *J. Am. Chem. Soc.* **122,** 10926–10942 (2000).
46. Ames, W. *et al.* Theoretical evaluation of structural models of the S_2 state in the oxygen evolving complex of photosystem II: protonation states and magnetic interactions. *J. Am. Chem. Soc.* **133,** 19743–19757 (2011).

Acknowledgements

This work was supported by the California Institute of Technology, the Searle Scholars Program, an NSF CAREER award (CHE-1151918 to T.A.) and the NSF Graduate Research Fellowship Program (to E.Y.T.). The authors thank L.M. Henling and D.E. Herbert for assistance with crystallography, and P-H. Lin for assistance with magnetic susceptibility studies. The Bruker KAPPA APEXII X-ray diffractometer was purchased with an NSF Chemistry Research Instrumentation award to Caltech (CHE-0639094). The X-ray spectroscopy work was supported by the NIH (grant no. F32GM100595 to R.T.) and by the Director of the Office of Basic Energy Science (OBES), Division of Chemical Sciences, Geosciences, and Biosciences, DOE (contract no. DE-AC02-05CH11231 to J.Y.). Synchrotron facilities were provided by the Stanford Synchrotron Radiation Lightsource (SSRL), operated by the DOE, OBER.

Author contributions

E.Y.T. and T.A. designed the research. E.Y.T. and R.T. performed the experiments. R.T. and J.Y. provided XANES characterization. E.Y.T., R.T., J.Y. and T.A. analysed data. E.Y.T. and T.A. wrote the paper.

Additional information

Supplementary information is available in the online version of the paper. Reprints and permissions information is available online at www.nature.com/reprints. Correspondence and requests for materials should be addressed to T.A.

Competing financial interests

The authors declare no competing financial interests.